

Revealing massive black hole astrophysics: The potential of hierarchical inference with extreme mass-ratio inspiral observations

SHASHWAT SINGH ,¹ CHRISTIAN E. A. CHAPMAN-BIRD ,² CHRISTOPHER P. L. BERRY ,¹ AND JOHN VEITCH ¹

¹*Institute for Gravitational Research, University of Glasgow, Kelvin Building, University Ave., Glasgow, G12 8QQ, United Kingdom*

²*Institute for Gravitational Wave Astronomy & School of Physics and Astronomy, University of Birmingham, Edgbaston, Birmingham B15 2TT, United Kingdom*

ABSTRACT

Gravitational waves from extreme mass-ratio inspirals (EMRIs) will enable sub-percent measurements of massive black hole parameters and provide access to the demographics of compact objects in galactic nuclei. During the *LISA* mission, multiple EMRIs are expected to be detected, allowing statistical studies of massive black hole populations and their formation pathways. We perform hierarchical Bayesian inference on simulated EMRI catalogues to assess how well *LISA* could constrain the astrophysical population using parametrised population models. We test our inference framework on a variety of populations, including heterogeneous and homogeneous mixtures of parametrised sub-populations, and scenarios in which the assumed model is deliberately misspecified. Our results show that population parameters governing distributions with sharp features can be tightly constrained. Mixed populations can be disentangled with as few as ~ 20 detections, and even with model misspecification, the inference retains sensitivity to key population features. These results demonstrate the capabilities and limitations of EMRI population inference, providing guidance for constructing realistic astrophysical population models for *LISA* analysis.

Keywords: Gravitational wave astronomy (675) — Gravitational wave sources (677) — Supermassive black holes (1663) — Hierarchical models (1925)

1. INTRODUCTION

Observations reveal a correlation between the properties of massive black holes (MBHs) and their host galaxies (D. Richstone et al. 1998; L. Ferrarese & D. Merritt 2000; J. Kormendy & L. C. Ho 2013). Despite this apparent ubiquity of their co-evolution, the origins and growth of MBHs remain poorly understood (M. Volonteri et al. 2021; D. M. Alexander et al. 2025). Although new observations from *JWST* shed light on MBHs accretion in the form of active galactic nuclei (AGNs; V. Kokorev et al. 2023; G. Zucchi et al. 2025; W. Ren et al. 2025; Y. Harikane et al. 2023), the vast majority of MBHs are electromagnetically quiescent. The *Laser Interferometer Space Antenna* (*LISA*) mission will help to fill this gap; it will detect gravitational waves (GWs) from the merger of black holes across a broad spectrum of masses and redshifts, complementing current electromagnetic observations.

Email: s.singh.3@research.gla.ac.uk

In low-to-intermediate mass galaxies ($\sim 10^8$ – $10^{12} M_{\odot}$), MBHs are often found co-existing with dense nuclear stellar clusters (NSCs), which provide a reservoir for compact objects (COs) such as stellar-mass black holes (sBHs), white dwarfs and neutron stars (A. W. Graham & L. Spitler 2009; I. Y. Georgiev et al. 2016; N. Neumayer et al. 2020). The dynamical evolution of such COs in the NSC is driven by the gravitational potential of the MBH and its environment. A small fraction of COs can become gravitationally bound to the MBH, forming a highly asymmetric-mass binary (P. Amaro-Seoane 2018). Such a binary system is known as an extreme mass-ratio inspiral (EMRI). As the CO gradually loses energy and angular momentum through the emission of GWs (P. Amaro-Seoane et al. 2007; C. P. L. Berry et al. 2019), the orbit shrinks slowly. Due to this mass ratio of the binary, an EMRI can spend $\sim 10^5$ – 10^6 orbital cycles in the millihertz band ($\sim 10^{-4}$ – 10^{-1} Hz), where *LISA* is most sensitive (M. Colpi et al. 2024). The long-lived and information-rich GW signals enable constraints on the MBH and CO masses, MBH spin, and orbital eccentricity and inclination of the orbital

plane within $\sim 0.001\%$ accuracy (L. Barack & C. Cutler 2004; S. Babak et al. 2017; C. E. A. Chapman-Bird et al. 2025). These sub-percent precision measurements of EMRI parameters will offer a unique opportunity to explore the MBH population (J. R. Gair 2009; S. Babak et al. 2017).

Several EMRI formation mechanisms have been proposed depending on the MBH environment. In dense NSCs, COs can be scattered onto high-eccentricity and low-angular-momentum orbits due to gravitational interactions with the stellar background, leading to the formation of a binary with the MBH (J. Binney & S. Tremaine 1987). This mechanism of EMRI formation is known as the loss-cone channel (A. P. Lightman & S. L. Shapiro 1977; T. Alexander 2017a), and it leads to gradual orbital decay via GW emission during successive periapsis passages (D. Merritt 2013). Beyond stellar dynamics, the MBH environment plays a critical role in regulating EMRIs formation. The presence of gas (Z. Pan & H. Yang 2021; Z. Pan et al. 2021; Z. Lyu et al. 2024), or its absence (T. Alexander 2017b; Q. Cui et al. 2025), can alter the inclination of the orbital plane and orbital eccentricity of the CO, influencing the EMRI rate. For example, AGN discs could provide an efficient in-situ channel where COs form, migrate and inspiral within the disc under the influence of gas drag and disc torques (Y. Levin 2007; Z. Pan & H. Yang 2021; L. Speri et al. 2023). Additional astrophysical factors, such as starbursts (Y. Levin 2007) or supernova explosions (E. Bortolas et al. 2017; E. Bortolas & M. Mapelli 2019), could further enhance EMRI formation rates. EMRIs could also form from the tidal capture of one component of a stellar-mass binary (M. C. Miller et al. 2005; X. Chen & W.-B. Han 2018; Y. Raveh & H. B. Perets 2021). In such systems, one of the component CO could be ejected while the other remains bound to the MBH, forming an EMRI. MBH binaries could also induce EMRI formation (G. Mazzolari et al. 2022), where the COs act as mediators to bring MBH binaries to parsec-scales (P. A. Seoane et al. 2023, Sec. 2.2). Hence, given the variety and complexity of the astrophysical processes influencing EMRI formation, and the current absence of direct observational constraints, these astrophysical processes and their relative contribution to the total EMRI rate remain poorly constrained (P. A. Seoane et al. 2023).

By combining multiple EMRI observations, it may be possible to constrain both the astrophysical processes governing EMRI formation and their relative contributions to the overall population (J. R. Gair et al. 2010; C. E. A. Chapman-Bird et al. 2023). To extract the astrophysical parameters governing the various astrophys-

ical processes, we need to perform a population-level (*hierarchical*) inference, accounting for selection effects and the uncertainties in individual EMRI parameter measurements (I. Mandel et al. 2019; S. Vitale et al. 2022).

Selection effects are important because the detected EMRI population is not an accurate representation of the underlying astrophysical population. Detection efficiency varies strongly across EMRI parameter space and is primarily dictated by the signal-to-noise ratio (SNR). Hence, population inference must explicitly account for these biases to avoid incorrect inference. In the absence of any standardised EMRI detection pipeline, the detectability is commonly modelled as a function of SNR (J. R. Gair et al. 2004, 2010; S. Babak et al. 2017), equivalent to defining an SNR-limited catalogue. An SNR-based selection function quantifies the probability of detecting an event from a given population model, hence factoring in the undetected events (I. Mandel et al. 2019; S. Vitale et al. 2022). Accurately evaluating this selection function, however, presents a challenge. It requires computing a large ensemble of EMRI SNRs for a given population model, which in turn requires repeated waveform generation. This step is a critical computational bottleneck in population inference. Even with accelerated computation on graphics processing units (C. E. A. Chapman-Bird et al. 2025), generating a single 6-year waveform takes a couple of seconds, making direct evaluation of the selection function computationally prohibitive. To overcome this challenge, machine-learning (ML)-based emulation, pioneered for EMRIs in C. E. A. Chapman-Bird et al. (2023) and further extended in S. Singh et al. (2025), has been developed to address this problem. Incorporating such ML-based emulators into the inference framework allows one to account for undetected events, leading to accurate constraints on the underlying population.

In this work, we apply this hierarchical inference framework to phenomenological population models representing the outcome from various formation channels. We begin by outlining our framework in Sec. 2. We then discuss our phenomenological population models in Sec. 3, and present results from hierarchical inference in Sec. 4, demonstrating the potential for constraining population parameters in a variety of scenarios. Finally, we conclude in Sec 5 discussing the scientific potential of *LISA* observations.

2. BAYESIAN HIERARCHICAL INFERENCE

We describe the astrophysical distribution of EMRIs with a population model $p_{\text{pop}}(\boldsymbol{\theta}|\boldsymbol{\Lambda})$, which gives the probability for single-event parameters $\boldsymbol{\theta}$ and is parametrised by the *hyperparameters* (population-level

parameters) $\boldsymbol{\Lambda}$. Hierarchical Bayesian inference combines multiple observations to infer $\boldsymbol{\Lambda}$, consistently accounting for the uncertainties arising from single-event parameter estimation. The goal is to estimate these hyperparameters using a catalogue of N_{det} detected EMRIs from the *LISA* data stream \mathbf{d} .

Using Bayes' theorem, we can express the *hyperposterior* (population-level posterior) as

$$p(\boldsymbol{\Lambda}|\mathbf{d}) = \frac{\pi(\boldsymbol{\Lambda})\mathcal{L}(\mathbf{d}|\boldsymbol{\Lambda})}{\mathcal{Z}(\mathbf{d})}, \quad (1)$$

where in the numerator, the first term $\pi(\boldsymbol{\Lambda})$ is the *hyperprior* for the population parameters, and the second term is the hyperlikelihood \mathcal{L} for our set of observed data \mathbf{d} , and the denominator is the *hyperevidence* \mathcal{Z} .

Each observed event $i \in [0, N_{\text{det}}]$ is described by source parameters $\boldsymbol{\theta}_i$ (Table 1). Under the assumption that detections are independent given the population model $p_{\text{pop}}(\boldsymbol{\theta}|\boldsymbol{\Lambda})$, the *hyperlikelihood* (I. Mandel et al. 2019; S. Vitale et al. 2022) can be expressed by marginalising over $\boldsymbol{\theta}_i$ as

$$\mathcal{L} = \prod_{i=1}^{N_{\text{det}}} \frac{\int d\boldsymbol{\theta}_i p(\mathbf{d}|\boldsymbol{\theta}_i)p_{\text{pop}}(\boldsymbol{\theta}_i|\boldsymbol{\Lambda})}{\alpha(\boldsymbol{\Lambda})} \times e^{-\mathcal{R}\alpha(\boldsymbol{\Lambda})} [\mathcal{R}\alpha(\boldsymbol{\Lambda})]^{N_{\text{det}}}. \quad (2)$$

Here, the product accounts for the marginalised likelihood of each detected event from the chosen population model $p_{\text{pop}}(\boldsymbol{\theta}|\boldsymbol{\Lambda})$ normalised by the selection function $\alpha(\boldsymbol{\Lambda})$. The second term accounts for the probability of detecting N_{det} events assuming a Poisson process with rate $\mathcal{R}\alpha$, where \mathcal{R} is the rate of EMRIs.

The selection function, $\alpha(\boldsymbol{\Lambda})$, is calculated by integrating the probability of detecting a system with given parameters $P_{\text{det}}(\boldsymbol{\theta})$ over the population (I. Mandel et al. 2019; S. Vitale et al. 2022),

$$\alpha(\boldsymbol{\Lambda}) = \int d\boldsymbol{\theta} P_{\text{det}}(\boldsymbol{\theta})p_{\text{pop}}(\boldsymbol{\theta}|\boldsymbol{\Lambda}). \quad (3)$$

This quantity represents the fraction of the underlying population that is detectable and enables the population-level inference without bias.

Following C. E. A. Chapman-Bird et al. (2023), we treat detectability solely as a function of SNR as

$$P_{\text{det}} = \mathcal{H}(\rho_n - \rho_t), \quad (4)$$

where ρ_n is a noise-realised SNR, \mathcal{H} is the Heaviside step function and ρ_t is a chosen threshold SNR. We obtain ρ_n^2 by drawing a sample from a non-central χ^2 distribution with two degrees of freedom and non-centrality parameter ρ_{opt}^2 (M. Maggiore 2007, Chapter 7), where ρ_{opt} is the optimal SNR.

We approximate the selection function in Eq. (3) by evaluating it as a Monte Carlo sum

$$\alpha(\boldsymbol{\Lambda}) \approx \frac{1}{N_t} \sum_{k=0}^{N_t} \overline{P_{\text{det}}}(\boldsymbol{\theta}_k), \quad (5)$$

where $\{\boldsymbol{\theta}_k\}$ are sampled from the population distribution $p_{\text{pop}}(\boldsymbol{\theta}|\boldsymbol{\Lambda})$ and $\overline{P_{\text{det}}} = 1 - P(\rho_n > \rho_t|\rho_{\text{opt}})$. To achieve a percent-level accuracy, one needs to compute $P_{\text{det}}(\boldsymbol{\theta}_k) \sim 10^5\text{--}10^6$ times, which is prohibitively expensive considering that $\alpha(\boldsymbol{\Lambda})$ must be evaluated a similar number of times during a typical population inference.

To overcome this bottleneck in the selection function, we use `poplar` (C. Chapman-Bird & S. Singh 2025), a developed in C. E. A. Chapman-Bird et al. (2023) and further extended in S. Singh et al. (2025). C. E. A. Chapman-Bird et al. (2023) employed two *multi-layer perceptron* (MLP) neural networks (V. Acquaviva 2023, Sec. 8.2.1) to emulate (i) the SNR and (ii) the selection function. S. Singh et al. (2025) further extended and tested the framework, allowing for sources that may or may not plunge, and accounting for random plunges within the finite *LISA* observation window. Following this approach, we train the selection function MLPs to map from the astrophysical parameters $\boldsymbol{\Lambda}$ of our phenomenological population model to the selection function α . This framework provides orders-of-magnitude speed-ups in direct evaluations while enabling unbiased estimation of population parameters.

To estimate the hyperposterior $p(\boldsymbol{\Lambda}|\mathbf{d})$ in Eq. (2), we also need to evaluate the event-level likelihood for the i -th event $p(\mathbf{d}|\boldsymbol{\theta}_i)$. The EMRI parameters $\boldsymbol{\theta}_i$ can be extracted from the *LISA* data \mathbf{d} using event-level parameter-estimation methods. This requires generating a large ensemble of waveform realisations, which is computationally challenging for the case of EMRIs. For computational efficiency, we perform a Fisher matrix analysis where the likelihood is approximated as a multivariate Gaussian (M. Maggiore 2007, Chapter 7). This approximation is valid in the high-SNR regime, where the likelihood is well-approximated by a Gaussian around the true parameters (C. Cutler & E. E. Flanagan 1994; M. Vallisneri 2008). To account for the influence of noise, we randomly offset the maximum likelihood point from the true value, self-consistently using a distribution derived from the Fisher matrix evaluated at the true values (S. Stevenson et al. 2017; C. E. A. Chapman-Bird et al. 2023).

We impose an SNR threshold $\rho_t \geq 20$ motivated by previous studies on achievable detection thresholds for semi-coherent searches (J. R. Gair et al. 2010). While this choice is not driven by Fisher matrix requirements, Fisher-based estimates remain accurate at

Table 1. Phenomenological population models considered. Models A and B are shown explicitly, while mixed models ($A^{(1)} + A^{(2)}$, $A + B$, $B^{(1)} + B^{(2)}$) share the same functional form with a fixed branching fraction of $w = 0.7$. Each model corresponds to specific functional choices and hyperparameters, as detailed in Table 2.

Parameter θ_j	Description	Model A	Model B	Prior
$\log_{10}(M/M_\odot)$	Source-frame log MBH mass	Schechter	Power-law	[5, 10]
$\log_{10}(\mu/M_\odot)$	Source-frame log CO mass	Skew-normal	Power-law	[1, 2]
a	MBH spin	Beta	Truncated-Normal	[0.1, 0.7]
e_0	Initial eccentricity	Beta	Uniform	[0.1, 0.7]
p_0	Initial semi-latus rectum	-	-	$p_0(T_{\text{plunge}})$
ι	Inclination angle	Uniform	Uniform	$[\arccos(-1), \arccos(1)]$
θ_S	Polar sky location	Uniform	Uniform	$(0, \pi)$
ϕ_S	Azimuthal sky location	Uniform	Uniform	$(0, 2\pi)$
θ_K	Polar spin orientation	Uniform	Uniform	$(0, \pi)$
ϕ_K	Azimuthal spin orientation	Uniform	Uniform	$(0, 2\pi)$
d_L (Gpc)	Luminosity distance	Uniform in \mathcal{V}_c	Uniform in \mathcal{V}_c	(0, 10]
$\Phi_{\phi,0}, \Phi_{\theta,0}, \Phi_{r,0}$	Initial orbital phases	Uniform	Uniform	$(0, 2\pi)$
T_{plunge} (yr)	Plunge time since observation start	Uniform	Uniform	[1, 6]

this threshold. We calculate Fisher matrices using the `StableEMRIFisher` package (S. Kejriwal et al. 2026). We used the `Pn5AAK` waveform model for our analysis, implemented in the `FastEMRIWaveforms` package (A. J. K. Chua et al. 2021; M. L. Katz et al. 2021; L. Speri et al. 2024; C. E. A. Chapman-Bird et al. 2025). Following S. Singh et al. (2025), we adopt an observation window of four years where EMRI source may or may not plunge with random plunges mimicking realistic conditions. The waveforms are then modulated by the *LISA* response function using the first-generation time-delay interferometry configuration with equal arm lengths. While the choice of time-delay interferometry generation does not significantly impact our results, this setup demonstrates that realistic sky averaging can be naturally incorporated into our framework. We retain the *A* and *E* channels, as the *T* channel carries negligible strain content in this configuration, and compute the detector response using the `FastLISAResponse` module of the `lisa-on-gpu` package (M. L. Katz et al. 2022). Having calculated all the necessary quantities to compute the hyperlikelihood, we employ nested sampling using `nessai` (M. J. Williams 2021; M. J. Williams et al. 2021) to explore the hyperparameter space efficiently.

3. POPULATION DISTRIBUTION

We adopt a phenomenological approach to model the EMRI population $p_{\text{pop}}(\boldsymbol{\theta}|\boldsymbol{\Lambda})$, parametrising the logarithmic MBH ($\log_{10}(M/M_\odot)$; Sec. 3.1) and CO mass ($\log_{10}(\mu/M_\odot)$; Sec. 3.3); MBH spin (a ; Sec 3.2) and the initial eccentricity, which we defined at 6 years before the plunge (e_0 ; Sec 3.4).

We consider two representative EMRI population models, A and B, described in Table 1, which differ in complexity, and combine them to form mixed models: $A^{(1)} + A^{(2)}$, $A + B$, and $B^{(1)} + B^{(2)}$. Model A represents hierarchical and accretion-driven MBH growth and evolution motivated by (B. Y. Wang et al. 2025; D. Sijacki et al. 2015; M. Habouzit et al. 2021; R. S. Somerville et al. 2008), accompanied by mass segregation (J. N. Bahcall & R. A. Wolf 1977; T. Alexander 2017a) in galactic nuclei. Additionally, spins are consistent with efficient spin-up or spin-down through prolonged accretion and mergers (K. S. Thorne 1974; A. R. King & J. E. Pringle 2006). The eccentricity distribution reflects expectations for gradual circularisation in gas-rich nuclei (Z. Pan et al. 2021) or high eccentricities for other channels. In contrast, Model B represents a simplified scenario in which MBH growth is modelled using a power-law distribution for the MBH and CO masses, with the slope parameter governing the relative abundances of these masses (S. Babak et al. 2017; R. Abbott et al. 2021). MBH spin in Model B follows a narrow normal distribution signifying the overabundance of the dominant growth scenario, and we model eccentricities with a uniform distribution. These two models illustrate contrasting assumptions about EMRI populations, and serve as a foundation for exploring mixed formation scenarios and assessing the impact of model complexity on population predictions.

In the case of mixed models, we construct synthetic populations, such as $A + B$, by combining two distinct population models, thereby allowing us to explore the inference framework's ability to disentangle heterogeneous formation channels. Similarly, we create homo-

Table 2. Parametric forms used to model the underlying population distributions in this work. Each parameter $\theta_j \in \boldsymbol{\theta}$ is sampled from a distribution $p_{\text{pop}}(\theta_j | \boldsymbol{\Lambda})$, characterized by hyperparameters $\boldsymbol{\Lambda}$.

Distribution	Functional form $p_{\text{pop}}(\theta_j \boldsymbol{\Lambda})$	Hyperparameters $\boldsymbol{\Lambda}$
Beta	$\theta_j^{\alpha-1} (1 - \theta_j)^{\beta-1}$	α, β
Truncated-normal	$\exp[-(\theta_j - \mu)^2 / 2\sigma^2]$	μ, σ
Power-law	θ_j^λ	λ
Schechter	$x_c^{-1} (\theta_j/x_c)^\zeta \exp(-\theta_j \zeta/x_c)$	x_c
Skew-normal	$\exp(-\theta_j^2/2) [1 + \text{erf}(\gamma \theta_j / \sqrt{2})]$	γ

geneous mixed models ($A^{(1)} + A^{(2)}$ and $B^{(1)} + B^{(2)}$) by drawing two subpopulations from the same underlying model type but with contrasting hyperparameter values. These mixed models are constructed to test whether the framework can identify subpopulations within a single formation scenario with distinct hyperparameters or distinguish between completely different channels. For all analyses of mixed-population models, we fix the branching fraction at $w = 0.7$ for consistency. The mixed population is defined as

$$p_{\text{pop}}^{X+Y}(\boldsymbol{\theta} | \boldsymbol{\Lambda}) = w p_{\text{pop}}^X(\boldsymbol{\theta} | \boldsymbol{\Lambda}^X) + (1 - w) p_{\text{pop}}^Y(\boldsymbol{\theta} | \boldsymbol{\Lambda}^Y),$$

where $X, Y \in \{A, B\}$, and $\boldsymbol{\Lambda}^X, \boldsymbol{\Lambda}^Y$ refer to the hyperparameters of the respective specific submodels. These mixed models enable us to test astrophysically motivated scenarios that span different assumptions about MBH growth, CO mass spectra, and orbital dynamics. Representative functional forms are listed in Table 2 and the hyperprior ranges in Table 3.

3.1. MBH mass spectrum

The mass spectrum of MBHs is shaped by the distribution of initial seed masses and their subsequent growth through accretion and mergers (M. Volonteri et al. 2021). Multiple seed formation channels populate the early Universe with characteristic initial masses. Population III stars (R. S. Klessen 2019) in the early metal-free Universe set the initial black hole mass at $\sim 10^2$ – $10^3 M_\odot$ (A. Heger & S. E. Woosley 2002). In massive dark matter halos ($\sim 10^8 M_\odot$), conditions allow for direct collapse of gas leading to the formation of massive seeds of $\sim 10^5$ – $10^7 M_\odot$ (M. C. Begelman et al. 2006). Dense stellar clusters may experience runaway collisions of massive stars, potentially producing very massive stars that collapse into intermediate-mass black holes ($\sim 2 \times 10^2$ – $10^3 M_\odot$; S. F. Portegies Zwart et al. 2004; M. Mapelli 2016). These seeds subsequently grow through gas accretion and mergers, producing a mass distribution shaped by hierarchical galaxy assembly and feedback-regulated accretion.

To capture this diversity in our population models, we consider two alternative parameterisations for the MBH

mass distribution (Table 1). For we adopt a modified Schechter-like distribution (P. Schechter 1976) for Model A and a power-law distribution for Model B (S. Babak et al. 2017; E. Barausse et al. 2020; R. Abbott et al. 2021; M. Habouzit et al. 2021). These two distributions allow exploring the performance of the hierarchical inference framework given the presence or absence of structure in the MBH mass spectrum.

The Schechter distribution is widely used to describe galaxy and halo mass functions in hierarchical structure formation (W. H. Press & P. Schechter 1974; P. Schechter 1976). Hierarchical galaxy assembly and feedback-regulated accretion can produce a mass spectrum with a characteristic peak (B. Y. Wang et al. 2025; D. Sijacki et al. 2015). Since MBHs co-evolve with galaxies (R. S. Somerville et al. 2008), we adopt a modified Schechter distribution to model MBH mass distribution for Model A. In the inference, we vary the hyperparameter x_c , which represents the peak in MBH mass spectrum and fix the slope $\zeta = 7$ (Table 2). The prior range for x_c (Table 3) and the functional form is motivated by numerical simulations (B. Y. Wang et al. 2025; D. Sijacki et al. 2015; M. Habouzit et al. 2021) and semi-analytic models of MBH–galaxy co-evolution (R. S. Somerville et al. 2008).

In contrast, the slope parameter λ_M used for Model B reflects the relative abundance of light versus heavy MBHs. A positive slope $\lambda_M > 0$ favours heavier MBHs, while $\lambda_M < 0$ suggest abundance of lighter MBHs. We explore λ_M within a range (Table 3) consistent with both cosmological simulations (M. Habouzit et al. 2021; E. Barausse 2012) and empirical fits to GW source populations (S. Babak et al. 2017; R. Abbott et al. 2021).

By adopting these parametrizations, our population models remain physically motivated and robust across plausible formation channels. Additional processes such as metal-poor gas inflows (A. Lupi et al. 2014), galaxy interactions (M. Volonteri et al. 2003; P. F. Hopkins et al. 2006), feedback (A. C. Fabian 2012; T. Di Matteo et al. 2005) and GW kicks (J. G. Baker et al. 2008) could further modulate growth and alter the mass spectrum, but their inclusion is beyond the scope of our illustrative models.

Table 3. Hyperprior ranges for the population models considered in this work. Each column corresponds to the population models: single-component (A or B) or mixture models ($A^{(1)} + A^{(2)}$, $A + B$, $B^{(1)} + B^{(2)}$). For each hyperparameter $\Lambda_j \in \Lambda$, the hyperprior $\pi(\Lambda_j)$ is set as a uniform distribution with the range $\Lambda_j \in [\Lambda_{\min}, \Lambda_{\max}]$ specified. Superscripts A and B denote the component population in the mixed population model, while w is the branching fraction. A dash (–) indicates that a parameter is not included in the corresponding model.

Parameters θ	A	B	$A^{(1)} + A^{(2)}$	$A + B$	$B^{(1)} + B^{(2)}$
MBH mass	$x_c \in [6.5, 9.5]$	$\lambda_M \in [-3, -1.01]$	$x_c^{A^{(1)}} \in [6.5, 9.5]$ $x_c^{A^{(2)}} \in [6.5, 9.5]$	$x_c^A \in [6.5, 9.5]$ $\lambda_M^B \in [-3, -1.01]$	$\lambda_M^{A^{(1)}} \in [-3, -1.01]$ $\lambda_M^{B^{(2)}} \in [-3, -1.01]$
CO mass	$\gamma_\mu \in [-1, 1]$	$\lambda_\mu \in [-4, -1.5]$	$\gamma_\mu^{A^{(1)}} \in [-1, 1]$ $\gamma_\mu^{A^{(2)}} \in [-1, 1]$	$\gamma_\mu^A \in [-1, 1]$ $\lambda_\mu^B \in [-4, -1.5]$	$\lambda_\mu^{B^{(1)}} \in [-4, -1.5]$ $\lambda_\mu^{B^{(2)}} \in [-4, -1.5]$
Spin	$\alpha_a \in [10, 15]$	$\mu_a \in [0.1, 0.7]$	$\alpha_a^{A^{(1)}} \in [10, 15]$ $\beta_a^{A^{(1)}} \in [5, 10]$ $\alpha_a^{A^{(2)}} \in [10, 15]$ $\beta_a^{A^{(2)}} \in [5, 10]$	$\alpha_a^A \in [10, 15]$ $\beta_a^A \in [5, 10]$ $\mu_a^B \in [0.1, 0.7]$ $\sigma_a^B \in [0.001, 0.05]$	$\mu_a^{B^{(1)}} \in [0.1, 0.7]$ $\sigma_a^{B^{(1)}} \in [0.001, 0.05]$ $\mu_a^{B^{(2)}} \in [0.1, 0.7]$ $\sigma_a^{B^{(2)}} \in [0.001, 0.05]$
Eccentricity	$\alpha_e \in [5, 10]$	–	$\alpha_{e_0}^{A^{(1)}} \in [5, 10]$ $\beta_{e_0}^{A^{(1)}} \in [1, 5]$	$\alpha_{e_0}^A \in [5, 10]$ $\beta_{e_0}^A \in [1, 5]$	–
	$\beta_e \in [1, 5]$	–	$\alpha_{e_0}^{A^{(2)}} \in [5, 10]$ $\beta_{e_0}^{A^{(2)}} \in [1, 5]$	–	–
Weight	–	–	$w \in [0.001, 0.999]$	$w \in [0.001, 0.999]$	$w \in [0.001, 0.999]$

3.2. MBH spin

The spin of a MBH is closely linked to its evolutionary history. The two principal growth channels are gas accretion and hierarchical mergers, and the spin distribution encodes which process dominates (R. S. Beckmann et al. 2024; M. Volonteri et al. 2005). Spin evolution is not monotonic: MBHs can be spun up or down in an erratic manner, with the spin expected to change repeatedly throughout their lifetime.

To capture the complexity of MBH spin distributions arising from the interplay of accretion, mergers, and galaxy properties, we adopt phenomenological population models that are flexible enough to represent a wide range of astrophysical scenarios. For Model A, we use a beta distribution (D. Wysocki et al. 2019), where the hyperparameters α_a and β_a control the shape of the distribution. Configurations with $\alpha_a < \beta_a$ favour an abundance of low-spin MBHs expected when stochastic accretion dominates, whereas $\alpha_a > \beta_a$ produces a distribution biased toward high-spin MBHs consistent with prolonged coherent accretion. For Model B, we employ a truncated normal distribution (Table 1), which captures spins concentrated around a mean value μ_a with a characteristic spread σ_a , while enforcing the physical bounds $0 \leq a \leq 0.998$. This reflects scenarios where spins cluster around a characteristic value, where one mechanism dominates over the others. These choices offer flexibility to replicate the diverse spin distributions anticipated from the underlying astrophysical processes. The prior ranges for these hyperparameters (Table 3) are

informed by cosmological simulations and semi-analytic models of MBH evolution (A. Sesana et al. 2014; D. Izquierdo-Villalba et al. 2020).

The spin distribution can be influenced by various factors. Coherent accretion can efficiently spin up a MBH (to a maximum $a = 0.998$; K. S. Thorne 1974), whereas stochastic, randomly oriented accretion events drive the spin toward moderate values (A. R. King & J. E. Pringle 2006; E. Berti & M. Volonteri 2008; N. Fanidakis et al. 2011). MBH mergers can abruptly alter the spin, typically producing significant reorientations and either spin-up or spin-down depending on the mass ratio and orbital configuration, effectively erasing any memory of the progenitor spins (M. Dotti et al. 2010). The spin magnitude is expected to evolve with redshift (R. S. Beckmann et al. 2024; M. Volonteri et al. 2005; L. Sala et al. 2024), although we do not model this explicitly. At higher redshifts, gas-rich environments spin up the MBH, while at lower redshifts the spin evolution diverges depending on MBH mass (M. Volonteri et al. 2013). Given these competing effects, the true population shape could exhibit skewness or tails. For this study, we therefore adopt flexible population models, including a beta distribution that can model strong boundary concentrations and skewness, as well as a truncated normal distribution that captures clustering around a characteristic value.

3.3. CO mass spectrum

NSCs, which host an abundance of such COs, provide the natural reservoir for EMRI formation. However, only a small fraction of these COs will form an EMRI.

A key mechanism that sustains the supply of COs near the MBH is mass segregation: a two-body relaxation process where the heavier CO, such as sBHs, sinks towards the galactic nucleus, pushing the lighter objects, such as stars, outward (J. N. Bahcall & R. A. Wolf 1977; T. Alexander 2017a). This affects the mass distribution of stellar COs in the NSC (C. Hopman & T. Alexander 2006; D. Aharon & H. B. Perets 2016; P. Amaro-Seoane & M. Pretor 2011). Depending upon the abundance of COs, mass segregation can fall into one of the two branches: weak (J. N. Bahcall & R. A. Wolf 1977) and strong (T. Alexander & C. Hopman 2009) regimes. Strong mass segregation follows in the scarcity of heavy CO, undergoing scattering with the lighter components before sinking towards the centre due to dynamical friction against the sea of lighter objects, developing a quasi-steady state (K. Kaur & H. B. Perets 2024; M. Pretor & P. Amaro-Seoane 2010). Conversely, in the weak regime, heavy COs are relatively abundant and undergo minimal interactions with the lighter objects, behaving as a single-mass population. We model this relative abundance in Model A using a truncated skew-normal distribution. The hyperparameter γ_μ controls the skewness of the distribution: $\gamma_\mu < 0$ corresponds to a scarcity of heavy sBHs, reflecting a strong regime, while $\gamma_\mu > 0$ indicates an abundance of more massive sBHs, as expected in the weak regime. For comparison, in Model B, we adopt a power-law distribution (R. Abbott et al. 2021). The slope of the power-law λ_μ governs the relative abundance of COs: $\lambda_\mu > 0$ favours more massive sBHs, while $\lambda_\mu < 0$ suppresses their presence in the NSC.

For both the models, we restrict our analysis to sBHs in the range $10M_\odot$ – $100 M_\odot$ (J. R. Gair et al. 2004).

3.4. Initial Eccentricity

For the case of EMRIs, high initial eccentricities (> 0.99) are expected during the relaxation (P. Amaro-Seoane et al. 2007; L. Broggi et al. 2022; D. Mancieri et al. 2025). However, much of it will be lost in orbital evolution before the signal enters the *LISA* band (P. C. Peters & J. Mathews 1963), broadening the distribution (P. Amaro-Seoane 2021). Initial eccentricities strongly depend on the formation channel. COs captured through two-body relaxation typically begin on extremely eccentric orbits (e.g., $e_0 > 0.9$), as they are scattered onto plunging trajectories with small periape-

sis radii (P. Amaro-Seoane et al. 2007; T. Alexander 2017a). In contrast, objects embedded in AGN discs often undergo significant circularisation due to viscous torques and gas dynamical friction, resulting in nearly circular orbits by the time they enter the *LISA* band (Z. Pan & H. Yang 2021). Binaries that are tidally separated (b-EMRIs) are expected to have low ($e_0 < 0.01$) to moderate ($e_0 < 0.1$) eccentricities (M. C. Miller et al. 2005). Even with effective circularisation, eccentricities may remain measurable, depending on their initial conditions and inspiral timescales. This eccentricity, hence, becomes a powerful diagnostic: highly eccentric inspirals suggest a dynamical origin, whereas circular EMRIs are more consistent with disc migration scenarios.

To capture the diversity of EMRI eccentricities arising from different scenarios, we model the eccentricity distribution with a beta distribution (Table 1) for Model A and a uniform distribution for Model B. For Model A, the hyperparameters α_{e_0} and β_{e_0} control the relative weight of high versus low-eccentric systems. Configurations with $\alpha_{e_0} > \beta_{e_0}$ represent populations dominated by dynamical capture through two-body relaxation, where highly eccentric orbits are typical, whereas $\alpha_{e_0} < \beta_{e_0}$ corresponds to scenarios producing predominantly low eccentricities, such as EMRIs embedded in AGN discs or b-EMRIs from binary tidal separations. In contrast, Model B assumes a uniform distribution (Table 1), representing the case where no single formation channel dominates, and eccentricities are spread with equal probabilities across the full physical range.

There are several other factors that could influence EMRI eccentricities. Environmental effects such as stellar scattering, mass segregation, and resonant relaxation (M. A. Gurkan & C. Hopman 2007) can modify orbital eccentricity before GW emission dominates (L. Broggi et al. 2022). Eccentricity evolution is also expected to depend on the redshift and mass of the central MBH (P. Amaro-Seoane 2018). While these effects are not modelled here, they represent a potential extension for future work.

3.5. Inclination, Luminosity Distance

Our baseline assumption is that the inclination angle ι_0 is uniformly distributed in $\cos \iota_0 \in [-1, 1]$, where positive (negative) values correspond to prograde (retrograde) orbits. While this is a common choice (P. Amaro-Seoane et al. 2007; J. R. Gair et al. 2010) for isotropic populations, it is a simplification. In realistic environments, inclination distributions can be strongly biased by formation channels and local dynamics. For example, EMRIs forming in AGN discs are expected to align with the disc plane due to gas torques and migration, favour-

ing low inclinations relative to the disc axis (Z. Pan & H. Yang 2021; Z. Lyu et al. 2024). Similarly, mass segregation in dense stellar clusters can lead to preferential capture of objects on prograde orbits around spinning MBHs, while resonant relaxation may introduce mild anisotropies (C. Hopman & T. Alexander 2006; T. Alexander & C. Hopman 2009; T. Alexander 2017a). These effects could produce non-uniform inclination distributions (F. Zhang & P. A. Seoane 2025), particularly in galactic nuclei with significant rotation or disc structure. Incorporating such correlations between inclination and environment is beyond the scope of this work, but represents an important extension for future studies.

For luminosity distance, we distribute sources uniformly in comoving volume, up to a luminosity distance of $d_L = 10$ Gyr, assuming a Λ -cold dark matter cosmology with $\Omega_M = 0.3$ and $\Omega_\Lambda = 0.7$. This neglects any redshift evolution of the source population. The EMRI population is likely to evolve with redshift as both the distribution of MBHs and COs changes across cosmic time. Therefore, incorporating more realistic redshift distributions (V. Gennari et al. 2025), potentially correlated with other parameters, is important for precision modelling. We leave studying these potential correlations for future work, as they require more sophisticated population models.

4. POPULATION INFERENCE

We conduct a case-by-case study for the population models discussed in Sec. 3. The default results presented are for 10^4 injections, but the figures also show results from smaller injection sets (10^2 and 10^3) for comparison. The fraction of detected events remains consistent across the number of injections, staying within the range ~ 17 – 21% given the SNR threshold of 20.

First (Sec. 4.1), we test our inference framework on single-component populations (Models A and B) to verify its ability to accurately recover injected hyperparameters. Next (Sec. 4.2), we consider mixed populations constructed in two ways: (i) heterogeneous mixtures combining distinct astrophysical models (A + B), and (ii) homogeneous mixtures using the same functional form but extreme hyperparameter values ($A^{(1)} + A^{(2)}$, $B^{(1)} + B^{(2)}$). This mixture of heterogeneous and homogenous population models allows us to investigate whether we can differentiate between contrasting population models. Finally (Sec. 4.3), we test model *misprediction* by inferring populations with an incorrect population model. We inferred Model A+B using Models A and B separately, and similarly, Model A (B) using Model B (A) and A+B. These checks enable us to investigate what would happen in a plausible scenario where

a parametrised population model does not accurately reflect the underlying astrophysical population.

4.1. Inference on individual population models (A, B)

The posterior predictive distribution (PPD) describes the distribution of new, unobserved data, given the observed data, and accounts for uncertainty in the model parameters. It is obtained by marginalising the likelihood over the posterior distribution of the parameters. In Figure 1 and Figure 2, we show the posterior predictive distributions and the recovered one-dimensional posterior for Models A and B, respectively. The injected (true) values lie well within the inferred 90% credible intervals. As expected, increasing the number of EMRI injections significantly tightens the posterior distributions, improving the precision of the recovered hyperparameters. This confirms the consistency of the inference pipeline when the population model matches the underlying distribution.

Posterior predictive distribution plots also confirm the same trend. The uncertainty in the recovered hyperparameters approximately follows the expected $\propto 1/\sqrt{N_{\text{det}}}$ scaling with the number of detections N_{det} . Constraints tighten rapidly between 10^2 and 10^3 injections, with gradual improvement for higher injections, and the rate of improvement diminishes with larger sample sizes. However, even with 10^2 injections (18 detections), we recover well-informed posteriors.

For Model A, the hyperparameter representing the peak of the MBH mass spectrum x_c is recovered within 1.5% uncertainty for 10^4 injections (1886 detections), indicating a tight constraint. By comparison, the spin hyperparameters α_a and β_a and the eccentricity parameters α_{e0} and β_{e0} are recovered with larger fractional errors, though still well constrained. We recover α_a and β_a within $\sim 2\%$ and $\sim 3\%$, and α_{e0} and β_{e0} within $\sim 3\%$ and $\sim 4\%$. The relative abundance of COs in the NSC, represented in Model A as γ_μ , is recovered within $\sim 8\%$, which is the worst for this population model. Overall, we observe that for Model A, the parameters directly related to the MBH: the peak of the mass spectrum and its shape parameters governing the spin distribution, are recovered with the highest precision across all injection sets. This highlights that EMRI observations are particularly sensitive to the MBH mass and the spin.

For Model B, hyperparameters governing the MBH spin are well constrained, with sub-percent fractional uncertainty. This demonstrates that an abundance of a specific range of spin parameters will leave a clear imprint on the MBH spin, allowing for sub-percent recovery even for relatively small numbers of detected events (21). The slope of the MBH and CO mass λ_M and λ_μ

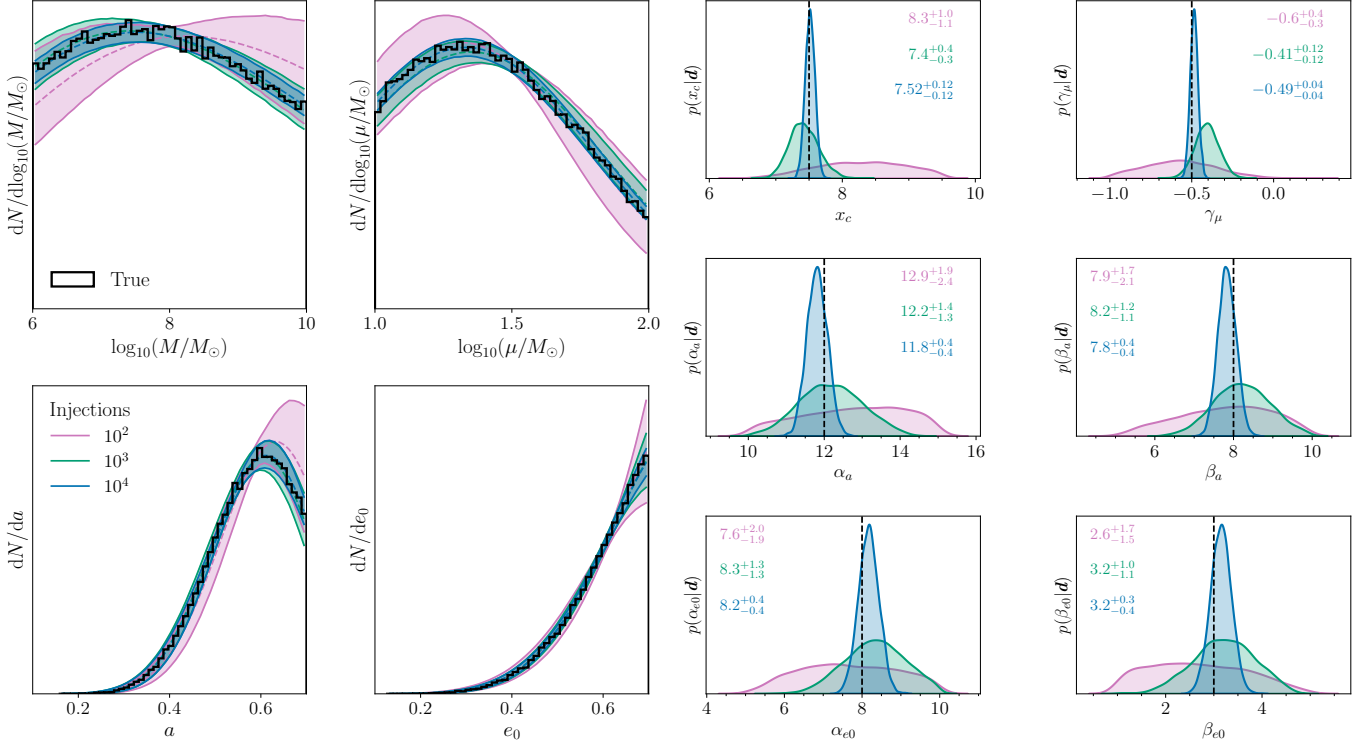


Figure 1. Posterior predictive distributions (*left*) and one-dimensional hyperparameter posteriors (*right*) for Model A. In the predictive distribution panels, the coloured solid curves denote the 90-th percentile and the dashed curves denote the mean. The colour scheme is consistent across panels: pink, green, and blue correspond to 10^2 , 10^3 , and 10^4 EMRI injections, respectively. For each set of injections 10^2 , 10^3 , and 10^4 for these simulations we detect 18, 188 and 1886 events, respectively. The solid black curve shows the true distribution reconstructed from the injected hyperparameters, whose values are marked by the vertical black dashed lines in the one-dimensional posteriors. The predictive distributions display the differential number density $dN/d\theta_i$ for $\theta_i \in \{\log_{10}(M/M_\odot), \log_{10}(\mu/M_\odot), a, e_0\}$, with symbols defined in Table 1. The one-dimensional posteriors summarise the inferred hyperparameters from the hierarchical population analysis. Each subplot on the *right* reports the median and associated 90% uncertainties, with colours indicating the number of injected events. The horizontal axis spans the relevant portion of the prior.

are recovered within $\sim 4\%$ for 10^4 injections (2080 detections).

Comparing the two population models, differences in parameter precision primarily reflect the structure of the underlying distributions. In Model A, the MBH and the CO mass spectra exhibit characteristic features: the MBH mass distribution peaks at x_c , and the CO skewness parameter γ_μ follows the injected high abundance of low-mass sBHs. This feature enables their recovery with high precision. By contrast, both in Model B are simple power laws, which lack sharp features and are consequently harder to constrain. Furthermore, the MBH spin distribution in Model A is described by a beta distribution, which is more flexible than the Gaussian-like spin distribution adopted in Model B and therefore results in larger fractional uncertainties, whereas the narrower Gaussian-like MBH spin distribution in Model B allows sub-percent precision. Hence, hyperparameters that control sharply defined features are consistently inferred with higher accuracy, whereas hyperparame-

ters governing broad distributions yield correspondingly weaker constraints (D. Chakrabarty et al. 2003; M. Fishbach & D. E. Holz 2020).

4.2. Inference on model mixtures ($A + B$, $A^{(1)} + A^{(2)}$, $B^{(1)} + B^{(2)}$)

We present our results for the heterogeneous population Model $A + B$ in Figure 3. The hyperparameters associated with the same physical parameters in the two components exhibit weak correlations. Since the Model A component contributes 70% to this mixed model, we observe that the hyperparameters of Model A, which are restricted to the MBH mass and spin, are well constrained. The mass hyperparameters of MBH mass and spin: x_c^A and α_a^A , β_a^A are recovered with less than the fractional uncertainty of 2% and 4% respectively. While the spin hyperparameters, μ_a^B and σ_a^B of the Model B component are still recovered with sub-percent precision, the mass hyperparameters of the CO are poorly constrained, evident by the broadened posteriors of the

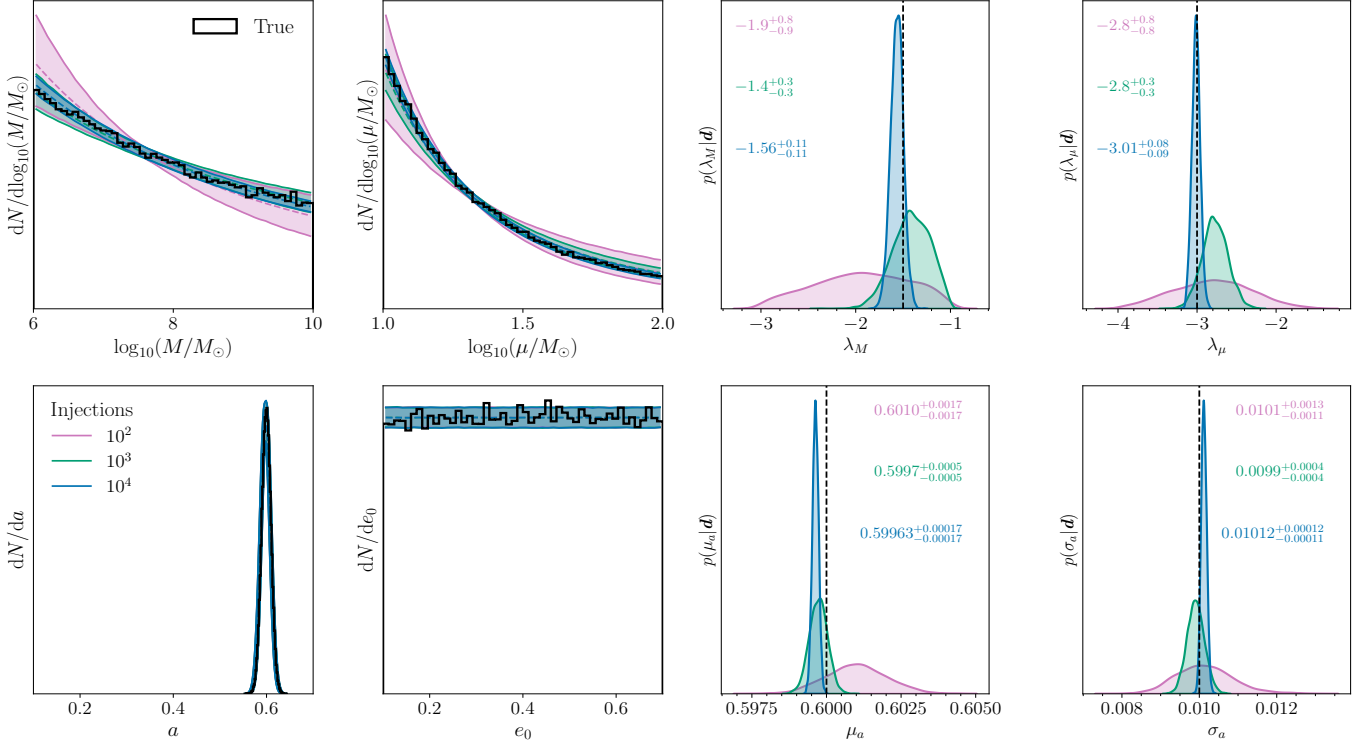


Figure 2. Posterior predictive distributions (*left*) and one-dimensional hyperparameter posteriors (*right*) for Model B. The plotting follows the same structure as Figure 1, where the only difference is the number of detections is 21, 206 and 2080, for 10^2 , 10^3 , and 10^4 injections, respectively.

Model B component. The branching fraction w is recovered within 2%, demonstrating that the framework is capable of differentiating between the two distinct population models.

For Model $A^{(1)} + A^{(2)}$, we recover hyperposteriors when the subpopulations differ significantly in their underlying hyperparameter values, rather than in their parameterisation (Figure 5 in Appendix A). This confirms that the framework can successfully detect population diversity even within a single model type, provided that the subpopulations are sufficiently distinct. The mass-related hyperparameters show broad posteriors and correlated regions between the mass hyperparameters of MBH ($x_c^{A^{(1/2)}}$) and CO ($\gamma_\mu^{A^{(1/2)}}$). Similarly, for Model $B^{(1)} + B^{(2)}$ (Figure 6 in Appendix A), mass hyperparameters are strongly correlated, and a larger uncertainty is associated with their estimation. However, we also observe bimodality for the spin hyperparameters and branching fraction. Each mode in the recovered posterior corresponds to the injected extremal values of the hyperparameters. Even though the mean spin hyperparameters ($\mu_a^{B^{(1/2)}}$) are recovered to within $\sim 1\%$, the corresponding variances ($\sigma_a^{B^{(1/2)}}$) exhibit substantially larger uncertainties of order $\sim 4\%$. This increased uncertainty also propagates to the branching fraction w ; this has a total uncertainty of $\sim 60\%$, although the

width of the single mode corresponds to an uncertainty of $\sim 2\%$. Although the parameters remain well constrained, the dual peaks cluster around the true injected values, indicating that the framework correctly identifies two underlying populations rather than averaging them out.

The convergence behaviour remains consistent across all mixed model cases. Increasing the number of injected events yields tighter constraints and sharper identification of subpopulation features. However, due to the presence of weak correlations between the hyperparameters associated with the same physical parameters, we expect the rate of improvement to deviate from $1/\sqrt{N_{\text{det}}}$. These results demonstrate that the inference framework remains robust for mixed populations and can resolve composite structure, even when the subpopulations share similar functional forms.

4.3. Inference under model misspecification

In this final experiment, we assess the robustness of the hierarchical inference framework to model misspecification. This is an important consideration given that real astrophysical populations are unlikely to be perfectly represented by any single model. We evaluate cases in which the inferred population model does not match the true underlying distribution. Specifically, we

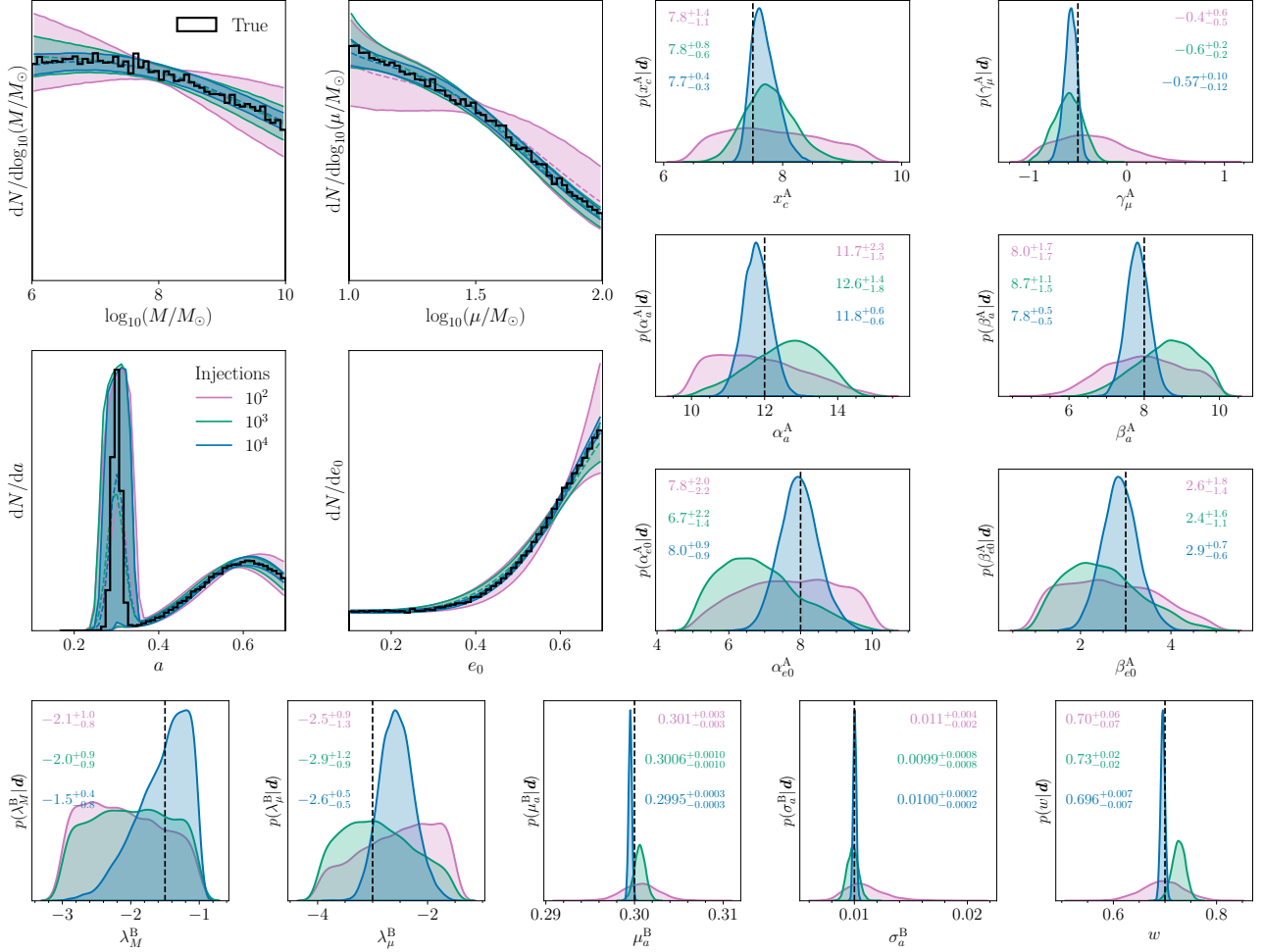


Figure 3. Posterior predictive distributions (*upper left*) and one-dimensional hyperparameter posteriors (*right* and *bottom*) for Model A + B. The plotting follows the same structure as Figure 1, where the only difference is the number of hyperparameters used to model the mixed population, where the number of detections is 19, 198 and 1980, for 10^2 , 10^3 , and 10^4 injections, respectively. Results for other mixed populations are shown in Appendix A.

infer Model A using Models B and A + B, and Model B using Models A and A + B. We also extend this analysis by using Model A and B separately to recover the mixed A + B population model. This allows us to quantify how an incorrect functional form biases the recovered hyperparameters and to assess whether key population features remain identifiable despite model mismatch.

We present our analysis in Figure 4, which highlights several systematic patterns that emerge under model mis-specification. Since in Model A + B, the Model A subpopulation is the dominant component (70%), we see that the mean of the reconstructed distribution closely matches the true distribution. We observe that the MBH mass, which follows a Schechter distribution, is well reconstructed compared to the power-law contribution of Model B, which is subdominant. This trend is also similar for the CO mass spectrum. The skewness γ_μ can be adjusted to account for the shape of the mixed

Model A + B population. However, we observe that the portion of the low-end CO mass spectrum which is modelled by B is not well reconstructed. A larger variance could potentially fit it, but the inferred distribution primarily reconstructs the dominant population. The reconstruction of the MBH and CO distribution improves with an increase in the number of injections, closely matching the true value.

While the MBH mass distribution is well reconstructed, this is not true for other distributions. The spin of the MBH and the eccentricity are poorly reconstructed. Since we are inferring the whole population model with a single component, the inference framework tends to average out the extremities. This is a behaviour we observe in the MBH spin where the mean of the beta distribution is skewed towards the median of the distribution. We also see that the reconstructed beta distribution is skewed towards the peak of the true Model A

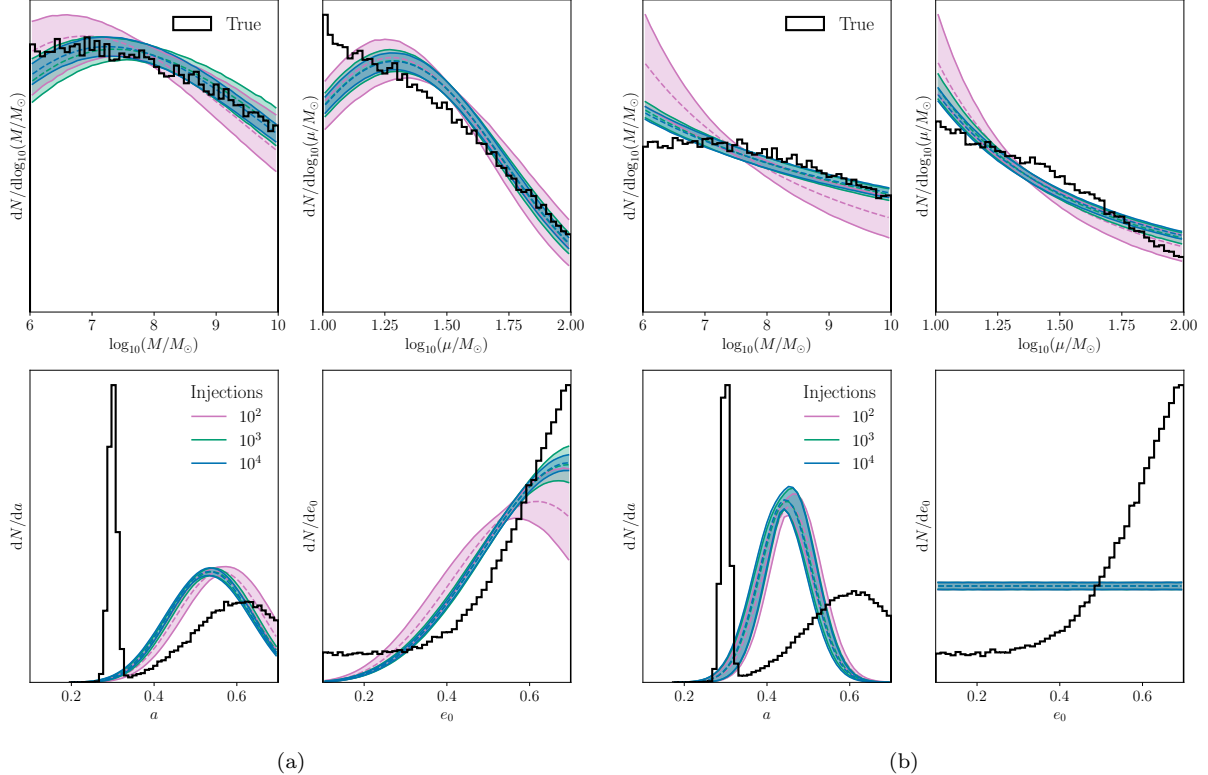


Figure 4. Posterior predictive distribution plots for the population Model A + B inferred with Model A (left) and B (right). The coloured solid curves denote the 90th percentile and the dashed curves denote the mean. The colour scheme is consistent across panels: pink, green, and blue correspond to 10^2 , 10^3 , and 10^4 EMRI injections, respectively. The solid black curve represents the true distribution reconstructed from the injected hyperparameters. We display the differential number density $dN/d\theta_i$ for $\theta_i \in \{\log_{10}(M/M_\odot), \log_{10}(\mu/M_\odot), a, e_0\}$, with symbols defined in Table 1.

component, resulting in $\beta_a < \alpha_a$, which corresponds to higher spins. This skewness reflects the influence of our modelling choice: inferring a mixed population model using a single-component model. A similar trend is observed for the CO mass spectrum. For eccentricities, we observe a similar feature, even though the averaging here is not immediately apparent. The hyperparameters of the beta distribution α_{e_0} and β_{e_0} are unable to fully recover the uniform part of the distribution. Instead, they adjust to partly capture the subdominant population, while still remaining skewed towards high eccentricity, which is the dominant component.

When recovering the Model A + B with Model B, we recover a similar trend. For the MBH mass distribution, the inferred power-law flattens to accommodate the strong high-mass contribution from Model A's Schechter-like distribution (peaked $\sim 10^7 M_\odot$). This adjustment biases the recovered distribution toward higher masses, preventing the accurate reconstruction of the lower-mass component. A similar trend is observed in the CO mass spectrum, where the slope also shifts to favour the dominant low-mass spectrum.

The MBH spin follows a similar trend when A + B is modelled with A such that the estimated mean is around the median of the distribution. Due to our uniform modelling of the eccentricity for Model B, it completely failed to capture the features present in the eccentricity distribution of Model A + B.

The reconstruction of Model A with A+B yields a better reconstruction compared to reconstructing Model A with B alone, for a similar reason that A has a dominant contribution in the A + B model. Both the mass parameters MBH and CO mass spectra are well reconstructed; however, the lower and higher ends of the spectrum show broadening in the 90th percentile lines, indicating the presence of a subdominant population. For the MBH spin distribution, the 90th percentile lines show significant bumps and broadening near the mean of the subdominant B component. In contrast, reconstruction using Model B, which has a completely different functional form, results in poor reconstruction. For the MBH and CO mass spectra, the true reconstructed distribution falls outside the 90th percentile mass spectrum regions, showcasing the difficulty of using a power law to fit a

distribution that possesses features. Similarly, for the MBH spin reconstruction, the estimated mean deviates by approximately 30% from the injected mean while the eccentricity remains unconstrained due to its uniform underlying distribution.

Conversely, when we infer Model B from Model A and A + B, the reconstruction is poor across all parameters. In both cases, the MBH and CO mass reconstructions attempt to capture the power-law structure in the data, whereas the inference for spin aims to capture the narrow peak in the spin distribution. However, neither Model A nor Model A + B successfully reconstructs a portion of the true spectrum. Despite the overall poor performance, the inferred spin distribution exhibits a skew toward higher values, partially mimicking the behaviour observed in the data. This behaviour is consistent across both models. The inference compensates by pushing parameters toward their extreme values, attempting to mimic the narrower true distribution within the broader functional family of Model A. This behaviour reflects the beta distribution's ability to reproduce the sharp central clustering of the truncated normal model.

These results demonstrate that population inference under model misspecification leads to systematic, model-dependent biases rather than purely statistical fluctuations. The nature and magnitude of these biases depend on both the true underlying population and the functional form adopted for inference. In particular, when the assumed function form lacks the flexibility to represent salient features of the true distribution, the inference compensates by shifting hyperparameters toward values that best approximate the dominant component of the population, often at the expense of subdominant features. As a result, the recovered distributions tend to track the most prominent structures in the data while smoothing over or misrepresenting secondary, subdominant components. We find recurring signatures in the posterior predictive distributions, including broadened credible intervals and shifts in the reconstructed means relative to the injected population. While such features do not, by themselves, uniquely diagnose model misspecification, their systematic appearance across different parameters and inference setups provides evidence of tension between the assumed model and the underlying population. Posterior predictive checks, therefore, offer a useful consistency test for assessing whether an inferred model adequately captures the observed data (R. Abbott et al. 2021; I. M. Romero-Shaw et al. 2022). Even under incorrect assumptions, however, the inference retains sensitivity to physical parameters, suggesting that EMRI population inference can still deliver

meaningful astrophysical insight, provided that priors and model families are carefully chosen.

5. CONCLUSION

With their sub-percent level of constraints on MBH and CO masses, MBH spin, and orbital eccentricity, EMRIs provide a promising opportunity to disentangle the MBH formation mechanisms. We have investigated how a set of EMRI observations can be used to infer the underlying astrophysical population. We use a Bayesian hierarchical inference framework that accounts for the selection biases, overcoming the associated computational obstacle by leveraging the ML `poplar` emulator to obtain unbiased estimates of the population hyperparameters (C. E. A. Chapman-Bird et al. 2023; S. Singh et al. 2025). We performed population inference using a combination of single-component (A and B) and mixed ($A^{(1)} + A^{(2)}$, A + B, $B^{(1)} + B^{(2)}$) population models for EMRI sources to explore what *LISA* could tell us about the EMRI source population.

For single-component population models A and B, our population inferences reliably recover the true hyperparameters with increasing precision as the number of detections grows. The constraining power is closely linked to the structure of the underlying distributions. Sharply defined features, such as the peak of the MBH mass spectrum in Model A (a Schechter distribution) or the narrow width of a Gaussian spin distribution, produce tight constraints. Broader distributions yield larger uncertainties. These results confirm that, in the absence of model mismatch, hierarchical inferences can extract population-level information from EMRI catalogues.

Considering the plausible scenario that the EMRI population comes from multiple channels, we also studied mixed populations. Results demonstrate that population inferences can identify and characterise composite structure, even when subpopulations share the same general functional forms. For heterogeneous mixtures (A + B), the inference can separate components with distinct astrophysical origins and parametrisations, recovering the branching fraction with percent-level accuracy for 10^2 injections (19 detections). For homogeneous mixtures ($A^{(1)} + A^{(2)}$, $B^{(1)} + B^{(2)}$), inferences can highlight internal diversity driven solely by contrasting hyperparameter values. In these cases, correlations and partial degeneracies naturally emerge between subpopulation parameters, but the parametrised population inference framework nonetheless retains sensitivity to multimodality and avoids collapsing to a single averaged solution when $\mathcal{O}(> 10^2)$ observations are available.

It is unlikely that a parametrised population model will precisely describe the true source population. Con-

sidering model misspecification, we find that systematic biases arise in predictable and physically interpretable ways. Complex models can partially mimic simpler ones by tuning hyperparameters across a wide range, whereas simpler models fail to reconstruct the full shape of more structured populations. The direction of these biases provides diagnostic signatures of functional mismatch, highlighting the importance of choosing flexible yet physically grounded population models. Despite incorrect assumptions, key population trends often remain detectable, underscoring the resilience of hierarchical inference and the scientific value of EMRI catalogues even when astrophysical modelling is imperfect.

These results collectively demonstrate the potential of EMRI observations. We find that hierarchical population inference is resilient: while incorrect functional assumptions lead to unsurprising systematic biases, inference results nonetheless preserve qualitative sensitivity to key astrophysical trends. This implies that, for future *LISA* data analyses, even simplified or phenomenological models can extract meaningful constraints on EMRI formation channels, provided that model selection is performed jointly with hierarchical inference. The consistent recovery and strong constraints on spin–eccentricity correlations, along with the ability to measure relative mixture weights across various scenarios, highlight how

future *LISA* observations can extract meaningful astrophysical constraints on EMRI formation channels, even when using simplified phenomenological models.

ACKNOWLEDGMENTS

We thank Jonathan Gair for useful discussions. SS acknowledges support from the University of Glasgow. CEAC-B acknowledges past support from STFC studentship 2446638, and current support from UKSA grant UKRI971.

Software: NumPy (C. R. Harris et al. 2020), SciPy (P. Virtanen et al. 2020), Matplotlib (J. D. Hunter 2007), PyTorch (A. Paszke et al. 2019), Nessai (M. J. Williams 2021), StableEMRIFisher (S. Kejriwal et al. 2026), poplar (C. Chapman-Bird & S. Singh 2025), FastEMRIWaveforms (C. Chapman-Bird et al. 2025), fastlisaresponse (M. L. Katz et al. 2022),

DATA AVAILABILITY

All data used in this work are available on Zenodo, and the hierarchical inference analysis scripts are available on GitHub.

REFERENCES

Abbott, R., et al. 2021 *Astrophys. J. Lett.*, 913, L7, doi: [10.3847/2041-8213/abe949](https://doi.org/10.3847/2041-8213/abe949)

Acquaviva, V. 2023, Machine Learning for Physics and Astronomy (Princeton, New Jersey: Princeton University Press)

Aharon, D., & Perets, H. B. 2016 *Astrophys. J. Lett.*, 830, L1, doi: [10.3847/2041-8205/830/1/L1](https://doi.org/10.3847/2041-8205/830/1/L1)

Alexander, D. M., et al. 2025
<https://arxiv.org/abs/2506.19166>

Alexander, T. 2017a *Ann. Rev. Astron. Astrophys.*, 55, 17, doi: [10.1146/annurev-astro-091916-055306](https://doi.org/10.1146/annurev-astro-091916-055306)

Alexander, T. 2017b *J. Phys. Conf. Ser.*, 840, 012019, doi: [10.1088/1742-6596/840/1/012019](https://doi.org/10.1088/1742-6596/840/1/012019)

Alexander, T., & Hopman, C. 2009 *Astrophys. J.*, 697, 1861, doi: [10.1088/0004-637X/697/2/1861](https://doi.org/10.1088/0004-637X/697/2/1861)

Amaro-Seoane, P. 2018 *Living Rev. Rel.*, 21, 4, doi: [10.1007/s41114-018-0013-8](https://doi.org/10.1007/s41114-018-0013-8)

Amaro-Seoane, P. 2021, in Handbook of Gravitational Wave Astronomy, ed. C. Bambi, S. Katsanevas, & K. D. Kokkotas (Singapore: Springer), 17, doi: [10.1007/978-981-15-4702-7_17-1](https://doi.org/10.1007/978-981-15-4702-7_17-1)

Amaro-Seoane, P., Gair, J. R., Freitag, M., et al. 2007 *Class. Quant. Grav.*, 24, R113, doi: [10.1088/0264-9381/24/17/R01](https://doi.org/10.1088/0264-9381/24/17/R01)

Amaro-Seoane, P., & Pretor, M. 2011 *Class. Quant. Grav.*, 28, 094017, doi: [10.1088/0264-9381/28/9/094017](https://doi.org/10.1088/0264-9381/28/9/094017)

Babak, S., Gair, J., Sesana, A., et al. 2017 *Phys. Rev. D*, 95, 103012, doi: [10.1103/PhysRevD.95.103012](https://doi.org/10.1103/PhysRevD.95.103012)

Bahcall, J. N., & Wolf, R. A. 1977 *Astrophys. J.*, 216, 883, doi: [10.1086/155534](https://doi.org/10.1086/155534)

Baker, J. G., Boggs, W. D., Centrella, J., et al. 2008 *Astrophys. J. Lett.*, 682, L29, doi: [10.1086/590927](https://doi.org/10.1086/590927)

Barack, L., & Cutler, C. 2004 *Phys. Rev. D*, 69, 082005, doi: [10.1103/PhysRevD.69.082005](https://doi.org/10.1103/PhysRevD.69.082005)

Barausse, E. 2012 *Mon. Not. Roy. Astron. Soc.*, 423, 2533, doi: [10.1111/j.1365-2966.2012.21057.x](https://doi.org/10.1111/j.1365-2966.2012.21057.x)

Barausse, E., Dvorkin, I., Tremmel, M., Volonteri, M., & Bonetti, M. 2020 *Astrophys. J.*, 904, 16, doi: [10.3847/1538-4357/abba7f](https://doi.org/10.3847/1538-4357/abba7f)

Beckmann, R. S., et al. 2024 *Mon. Not. Roy. Astron. Soc.*, 536, 1838, doi: [10.1093/mnras/stae2595](https://doi.org/10.1093/mnras/stae2595)

Begelman, M. C., Volonteri, M., & Rees, M. J. 2006 *Mon. Not. Roy. Astron. Soc.*, 370, 289, doi: [10.1111/j.1365-2966.2006.10467.x](https://doi.org/10.1111/j.1365-2966.2006.10467.x)

Berry, C. P. L., Hughes, S. A., Sopuerta, C. F., et al. 2019 *Bull. Am. Astron. Soc.*, 51, 42. <https://arxiv.org/abs/1903.03686>

Berti, E., & Volonteri, M. 2008 *Astrophys. J.*, 684, 822, doi: [10.1086/590379](https://doi.org/10.1086/590379)

Binney, J., & Tremaine, S. 1987, *Galactic Dynamics* (Princeton, New Jersey: Princeton University Press)

Bortolas, E., & Mapelli, M. 2019 *Mon. Not. Roy. Astron. Soc.*, 485, 2125, doi: [10.1093/mnras/stz440](https://doi.org/10.1093/mnras/stz440)

Bortolas, E., Mapelli, M., & Spera, M. 2017 *Mon. Not. Roy. Astron. Soc.*, 469, 1510, doi: [10.1093/mnras/stx930](https://doi.org/10.1093/mnras/stx930)

Broggi, L., Bortolas, E., Bonetti, M., Sesana, A., & Dotti, M. 2022 *Mon. Not. Roy. Astron. Soc.*, 514, 3270, doi: [10.1093/mnras/stac1453](https://doi.org/10.1093/mnras/stac1453)

Chakrabarty, D., Morgan, E. H., Munro, M. P., et al. 2003 *Nature*, 424, 42, doi: [10.1038/nature01732](https://doi.org/10.1038/nature01732)

Chapman-Bird, C., Chua, A. J., Hughes, S. A., et al. 2025, Data for Fast EMRI Waveforms Zenodo, doi: [10.5281/zenodo.15624459](https://doi.org/10.5281/zenodo.15624459)

Chapman-Bird, C., & Singh, S. 2025, poplar: Accelerating selection bias modelling with machine learning, v0.3 Zenodo, doi: [10.5281/zenodo.17897846](https://doi.org/10.5281/zenodo.17897846)

Chapman-Bird, C. E. A., Berry, C. P. L., & Woan, G. 2023 *Mon. Not. Roy. Astron. Soc.*, 522, 6043, doi: [10.1093/mnras/stad1397](https://doi.org/10.1093/mnras/stad1397)

Chapman-Bird, C. E. A., et al. 2025 <https://arxiv.org/abs/2506.09470>

Chen, X., & Han, W.-B. 2018 *Commun. Phys.*, 1, 53, doi: [10.1038/s42005-018-0053-0](https://doi.org/10.1038/s42005-018-0053-0)

Chua, A. J. K., Katz, M. L., Warburton, N., & Hughes, S. A. 2021 *Phys. Rev. Lett.*, 126, 051102, doi: [10.1103/PhysRevLett.126.051102](https://doi.org/10.1103/PhysRevLett.126.051102)

Colpi, M., et al. 2024 <https://arxiv.org/abs/2402.07571>

Cui, Q., Han, W.-B., & Pan, Z. 2025 *Phys. Rev. D*, 111, 103044, doi: [10.1103/PhysRevD.111.103044](https://doi.org/10.1103/PhysRevD.111.103044)

Cutler, C., & Flanagan, E. E. 1994 *Phys. Rev. D*, 49, 2658, doi: [10.1103/PhysRevD.49.2658](https://doi.org/10.1103/PhysRevD.49.2658)

Di Matteo, T., Springel, V., & Hernquist, L. 2005 *Nature*, 433, 604, doi: [10.1038/nature03335](https://doi.org/10.1038/nature03335)

Dotti, M., Volonteri, M., Perego, A., et al. 2010 *Mon. Not. Roy. Astron. Soc.*, 402, 682, doi: [10.1111/j.1365-2966.2009.15922.x](https://doi.org/10.1111/j.1365-2966.2009.15922.x)

Fabian, A. C. 2012 *Ann. Rev. Astron. Astrophys.*, 50, 455, doi: [10.1146/annurev-astro-081811-125521](https://doi.org/10.1146/annurev-astro-081811-125521)

Fanidakis, N., Baugh, C. M., Benson, A. J., et al. 2011 *Mon. Not. Roy. Astron. Soc.*, 410, 53, doi: [10.1111/j.1365-2966.2010.17427.x](https://doi.org/10.1111/j.1365-2966.2010.17427.x)

Ferrarese, L., & Merritt, D. 2000 *Astrophys. J. Lett.*, 539, L9, doi: [10.1086/312838](https://doi.org/10.1086/312838)

Fishbach, M., & Holz, D. E. 2020 *Astrophys. J. Lett.*, 891, L27, doi: [10.3847/2041-8213/ab7247](https://doi.org/10.3847/2041-8213/ab7247)

Gair, J. R. 2009 *Class. Quant. Grav.*, 26, 094034, doi: [10.1088/0264-9381/26/9/094034](https://doi.org/10.1088/0264-9381/26/9/094034)

Gair, J. R., Barack, L., Creighton, T., et al. 2004 *Class. Quant. Grav.*, 21, S1595, doi: [10.1088/0264-9381/21/20/003](https://doi.org/10.1088/0264-9381/21/20/003)

Gair, J. R., Tang, C., & Volonteri, M. 2010 *Phys. Rev. D*, 81, 104014, doi: [10.1103/PhysRevD.81.104014](https://doi.org/10.1103/PhysRevD.81.104014)

Gennari, V., Mastrogiovanni, S., Tamanini, N., Marsat, S., & Pierra, G. 2025 *Phys. Rev. D*, 111, 123046, doi: [10.1103/ftw9-7xd5](https://doi.org/10.1103/ftw9-7xd5)

Georgiev, I. Y., Böker, T., Leigh, N., Lützgendorf, N., & Neumayer, N. 2016 *Mon. Not. Roy. Astron. Soc.*, 457, 2122, doi: [10.1093/mnras/stw093](https://doi.org/10.1093/mnras/stw093)

Graham, A. W., & Spitler, L. 2009 *Mon. Not. Roy. Astron. Soc.*, 397, 2148, doi: [10.1111/j.1365-2966.2009.15118.x](https://doi.org/10.1111/j.1365-2966.2009.15118.x)

Gurkan, M. A., & Hopman, C. 2007 *Mon. Not. Roy. Astron. Soc.*, 379, 1083, doi: [10.1111/j.1365-2966.2007.11982.x](https://doi.org/10.1111/j.1365-2966.2007.11982.x)

Habouzit, M., Li, Y., Somerville, R. S., et al. 2021 *Mon. Not. Roy. Astron. Soc.*, 503, 1940, doi: [10.1093/mnras/stab496](https://doi.org/10.1093/mnras/stab496)

Harikane, Y., Zhang, Y., Nakajima, K., et al. 2023 *Astrophys. J.*, 959, 39, doi: [10.3847/1538-4357/ad029e](https://doi.org/10.3847/1538-4357/ad029e)

Harris, C. R., Millman, K. J., van der Walt, S. J., et al. 2020 *Nature*, 585, 357–362, doi: [10.1038/s41586-020-2649-2](https://doi.org/10.1038/s41586-020-2649-2)

Heger, A., & Woosley, S. E. 2002 *Astrophys. J.*, 567, 532, doi: [10.1086/338487](https://doi.org/10.1086/338487)

Hopkins, P. F., Hernquist, L., Cox, T. J., et al. 2006 *Astrophys. J. Suppl.*, 163, 1, doi: [10.1086/499298](https://doi.org/10.1086/499298)

Hopman, C., & Alexander, T. 2006 *Astrophys. J. Lett.*, 645, L133, doi: [10.1086/506273](https://doi.org/10.1086/506273)

Hunter, J. D. 2007 *Comput. Sci. Eng.*, 9, 90, doi: [10.1109/MCSE.2007.55](https://doi.org/10.1109/MCSE.2007.55)

Izquierdo-Villalba, D., Bonoli, S., Dotti, M., et al. 2020 *Mon. Not. Roy. Astron. Soc.*, 495, 4681, doi: [10.1093/mnras/staa1399](https://doi.org/10.1093/mnras/staa1399)

Katz, M. L., Bayle, J.-B., Chua, A. J. K., & Vallisneri, M. 2022 *Phys. Rev. D*, 106, 103001, doi: [10.1103/PhysRevD.106.103001](https://doi.org/10.1103/PhysRevD.106.103001)

Katz, M. L., Chua, A. J. K., Speri, L., Warburton, N., & Hughes, S. A. 2021 *Phys. Rev. D*, 104, 064047, doi: [10.1103/PhysRevD.104.064047](https://doi.org/10.1103/PhysRevD.104.064047)

Kaur, K., & Perets, H. B. 2024 *Astrophys. J.*, 977, 8, doi: [10.3847/1538-4357/ad89bd](https://doi.org/10.3847/1538-4357/ad89bd)

Kejriwal, S., Burke, O., Chapman-Bird, C., & Chua, A. J. K. 2026, StableEMRIFisher (SEF) Github. <https://github.com/perturber/StableEMRIFisher>

King, A. R., & Pringle, J. E. 2006 *Mon. Not. Roy. Astron. Soc.*, 373, L93, doi: [10.1111/j.1745-3933.2006.00249.x](https://doi.org/10.1111/j.1745-3933.2006.00249.x)

Klessen, R. S. 2019, in *Formation of the First Black Holes*, ed. M. Latif & D. Schleicher (Singapore: World Scientific), 67, doi: [10.1142/9789813227958_0004](https://doi.org/10.1142/9789813227958_0004)

Kokorev, V., Fujimoto, S., Labbe, I., et al. 2023 *Astrophys. J. Lett.*, 957, L7, doi: [10.3847/2041-8213/ad037a](https://doi.org/10.3847/2041-8213/ad037a)

Kormendy, J., & Ho, L. C. 2013 *Ann. Rev. Astron. Astrophys.*, 51, 511, doi: [10.1146/annurev-astro-082708-101811](https://doi.org/10.1146/annurev-astro-082708-101811)

Levin, Y. 2007 *Mon. Not. Roy. Astron. Soc.*, 374, 515, doi: [10.1111/j.1365-2966.2006.11155.x](https://doi.org/10.1111/j.1365-2966.2006.11155.x)

Lightman, A. P., & Shapiro, S. L. 1977 *Astrophys. J.*, 211, 244, doi: [10.1086/154925](https://doi.org/10.1086/154925)

Lupi, A., Colpi, M., Devecchi, B., Galanti, G., & Volonteri, M. 2014 *Mon. Not. Roy. Astron. Soc.*, 442, 3616, doi: [10.1093/mnras/stu1120](https://doi.org/10.1093/mnras/stu1120)

Lyu, Z., Pan, Z., Mao, J., Jiang, N., & Yang, H. 2024 <https://arxiv.org/abs/2501.03252>

Maggiore, M. 2007, *Gravitational Waves. Vol. 1: Theory and Experiments* (Oxford: Oxford University Press), doi: [10.1093/acprof:oso/9780198570745.001.0001](https://doi.org/10.1093/acprof:oso/9780198570745.001.0001)

Mancieri, D., Broggi, L., Bonetti, M., & Sesana, A. 2025 *Astron. Astrophys.*, 694, A272, doi: [10.1051/0004-6361/202452306](https://doi.org/10.1051/0004-6361/202452306)

Mandel, I., Farr, W. M., & Gair, J. R. 2019 *Mon. Not. Roy. Astron. Soc.*, 486, 1086, doi: [10.1093/mnras/stz896](https://doi.org/10.1093/mnras/stz896)

Mapelli, M. 2016 *Mon. Not. Roy. Astron. Soc.*, 459, 3432, doi: [10.1093/mnras/stw869](https://doi.org/10.1093/mnras/stw869)

Mazzolari, G., Bonetti, M., Sesana, A., et al. 2022 *Mon. Not. Roy. Astron. Soc.*, 516, 1959, doi: [10.1093/mnras/stac2255](https://doi.org/10.1093/mnras/stac2255)

Merritt, D. 2013 *Class. Quant. Grav.*, 30, 244005, doi: [10.1088/0264-9381/30/24/244005](https://doi.org/10.1088/0264-9381/30/24/244005)

Miller, M. C., Freitag, M., Hamilton, D. P., & Lauburg, V. M. 2005 *Astrophys. J. Lett.*, 631, L117, doi: [10.1086/497335](https://doi.org/10.1086/497335)

Neumayer, N., Seth, A., & Boeker, T. 2020 *Astron. Astrophys. Rev.*, 28, 4, doi: [10.1007/s00159-020-00125-0](https://doi.org/10.1007/s00159-020-00125-0)

Pan, Z., Lyu, Z., & Yang, H. 2021 *Phys. Rev. D*, 104, 063007, doi: [10.1103/PhysRevD.104.063007](https://doi.org/10.1103/PhysRevD.104.063007)

Pan, Z., & Yang, H. 2021 *Phys. Rev. D*, 103, 103018, doi: [10.1103/PhysRevD.103.103018](https://doi.org/10.1103/PhysRevD.103.103018)

Paszke, A., Gross, S., Massa, F., et al. 2019 arXiv e-prints, arXiv:1912.01703, doi: [10.48550/arXiv.1912.01703](https://doi.org/10.48550/arXiv.1912.01703)

Peters, P. C., & Mathews, J. 1963 *Phys. Rev.*, 131, 435, doi: [10.1103/PhysRev.131.435](https://doi.org/10.1103/PhysRev.131.435)

Portegies Zwart, S. F., Baumgardt, H., Hut, P., Makino, J., & McMillan, S. L. W. 2004 *Nature*, 428, 724, doi: [10.1038/nature02448](https://doi.org/10.1038/nature02448)

Press, W. H., & Schechter, P. 1974 *Astrophys. J.*, 187, 425, doi: [10.1086/152650](https://doi.org/10.1086/152650)

Preto, M., & Amaro-Seoane, P. 2010 *Astrophys. J. Lett.*, 708, L42, doi: [10.1088/2041-8205/708/1/L42](https://doi.org/10.1088/2041-8205/708/1/L42)

Raveh, Y., & Perets, H. B. 2021 *Mon. Not. Roy. Astron. Soc.*, 501, 5012, doi: [10.1093/mnras/staa4001](https://doi.org/10.1093/mnras/staa4001)

Ren, W., Silverman, J. D., Faisst, A. L., et al. 2025 *Mon. Not. Roy. Astron. Soc.*, 544, 211, doi: [10.1093/mnras/staf1709](https://doi.org/10.1093/mnras/staf1709)

Richstone, D., et al. 1998 *Nature*, 395, A14. <https://arxiv.org/abs/astro-ph/9810378>

Romero-Shaw, I. M., Thrane, E., & Lasky, P. D. 2022 *Publ. Astron. Soc. Austral.*, 39, e025, doi: [10.1017/pasa.2022.24](https://doi.org/10.1017/pasa.2022.24)

Sala, L., Valentini, M., Biffi, V., & Dolag, K. 2024 *Astron. Astrophys.*, 685, A92, doi: [10.1051/0004-6361/202348925](https://doi.org/10.1051/0004-6361/202348925)

Schechter, P. 1976 *Astrophys. J.*, 203, 297, doi: [10.1086/154079](https://doi.org/10.1086/154079)

Seoane, P. A., et al. 2023 *Living Rev. Rel.*, 26, 2, doi: [10.1007/s41114-022-00041-y](https://doi.org/10.1007/s41114-022-00041-y)

Sesana, A., Barausse, E., Dotti, M., & Rossi, E. M. 2014 *Astrophys. J.*, 794, 104, doi: [10.1088/0004-637X/794/2/104](https://doi.org/10.1088/0004-637X/794/2/104)

Sijacki, D., Vogelsberger, M., Genel, S., et al. 2015 *Mon. Not. Roy. Astron. Soc.*, 452, 575, doi: [10.1093/mnras/stv1340](https://doi.org/10.1093/mnras/stv1340)

Singh, S., Chapman-Bird, C. E. A., Berry, C. P. L., & Veitch, J. 2025 <https://arxiv.org/abs/2508.16399>

Somerville, R. S., Hopkins, P. F., Cox, T. J., Robertson, B. E., & Hernquist, L. 2008 *Mon. Not. Roy. Astron. Soc.*, 391, 481, doi: [10.1111/j.1365-2966.2008.13805.x](https://doi.org/10.1111/j.1365-2966.2008.13805.x)

Speri, L., Antonelli, A., Sberna, L., et al. 2023 *Phys. Rev. X*, 13, 021035, doi: [10.1103/PhysRevX.13.021035](https://doi.org/10.1103/PhysRevX.13.021035)

Speri, L., Katz, M. L., Chua, A. J. K., et al. 2024 *Front. Appl. Math. Stat.*, 9, doi: [10.3389/fams.2023.1266739](https://doi.org/10.3389/fams.2023.1266739)

Stevenson, S., Berry, C. P. L., & Mandel, I. 2017 *Mon. Not. Roy. Astron. Soc.*, 471, 2801, doi: [10.1093/mnras/stx1764](https://doi.org/10.1093/mnras/stx1764)

Thorne, K. S. 1974 *Astrophys. J.*, 191, 507, doi: [10.1086/152991](https://doi.org/10.1086/152991)

Vallisneri, M. 2008 *Phys. Rev. D*, 77, 042001, doi: [10.1103/PhysRevD.77.042001](https://doi.org/10.1103/PhysRevD.77.042001)

Virtanen, P., Gommers, R., Oliphant, T. E., et al. 2020 *Nat. Methods*, 17, 261, doi: [10.1038/s41592-019-0686-2](https://doi.org/10.1038/s41592-019-0686-2)

Vitale, S., Gerosa, D., Farr, W. M., & Taylor, S. R. 2022, in *Handbook of Gravitational Wave Astronomy*, ed. C. Bambi, S. Katsanevas, & K. D. Kokkotas (Princeton, New Jersey: Springer), 45, doi: [10.1007/978-981-15-4702-7_45-1](https://doi.org/10.1007/978-981-15-4702-7_45-1)

Volonteri, M., Haardt, F., & Madau, P. 2003 *Astrophys. J.*, 582, 559, doi: [10.1086/344675](https://doi.org/10.1086/344675)

Volonteri, M., Habouzit, M., & Colpi, M. 2021 *Nature Rev. Phys.*, 3, 732, doi: [10.1038/s42254-021-00364-9](https://doi.org/10.1038/s42254-021-00364-9)

Volonteri, M., Madau, P., Quataert, E., & Rees, M. J. 2005 *Astrophys. J.*, 620, 69, doi: [10.1086/426858](https://doi.org/10.1086/426858)

Volonteri, M., Sikora, M., Lasota, J.-P., & Merloni, A. 2013 *Astrophys. J.*, 775, 94, doi: [10.1088/0004-637X/775/2/94](https://doi.org/10.1088/0004-637X/775/2/94)

Wang, B. Y., Zhou, Y., Chen, W., et al. 2025 *Astrophys. J.*, 993, 199, doi: [10.3847/1538-4357/ae073e](https://doi.org/10.3847/1538-4357/ae073e)

Williams, M. J. 2021, nessai: Nested Sampling with Artificial Intelligence, latest Zenodo, doi: [10.5281/zenodo.4550693](https://doi.org/10.5281/zenodo.4550693)

Williams, M. J., Veitch, J., & Messenger, C. 2021 *Phys. Rev. D*, 103, 103006, doi: [10.1103/PhysRevD.103.103006](https://doi.org/10.1103/PhysRevD.103.103006)

Wysocski, D., Lange, J., & O'Shaughnessy, R. 2019 *Phys. Rev. D*, 100, 043012, doi: [10.1103/PhysRevD.100.043012](https://doi.org/10.1103/PhysRevD.100.043012)

Zhang, F., & Seoane, P. A. 2025 <https://arxiv.org/abs/2510.10821>

Zucchi, G., Ji, X., Madau, P., et al. 2025 arXiv e-prints, arXiv:2510.10772, doi: [10.48550/arXiv.2510.10772](https://doi.org/10.48550/arXiv.2510.10772)

APPENDIX

A. INFERENCE PLOTS FOR POPULATION MODELS $A^{(1)} + A^{(2)}$ AND $B^{(1)} + B^{(2)}$

Figures 5 and 6 present posterior predictive distributions and one-dimensional hyperparameter posteriors for the mixed-population models $A^{(1)} + A^{(2)}$ and $B^{(1)} + B^{(2)}$, respectively.

For Model $A^{(1)} + A^{(2)}$, the hyperposteriors confirm that the inference pipeline successfully distinguishes between two subpopulations within the same model type. While spin-related hyperparameters are inferred with sub-percent accuracy, mass-related hyperparameters exhibit broader posteriors and correlated regions, particularly between the MBH mass parameters ($x_c^{A^{(1/2)}}$) and CO mass parameters ($\gamma_\mu^{A^{(1/2)}}$).

For Model $B^{(1)} + B^{(2)}$, similar trends are observed: mass hyperparameters remain strongly correlated and less precisely constrained, while spin hyperparameters are recovered with high accuracy. The spin posteriors display bimodality, with each mode corresponding to the injected extremal values of the hyperparameters. This bimodality also propagates to the branching fraction w , which, despite being well constrained, shows two distinct peaks. These dual modes indicate that the framework correctly identifies the presence of two underlying populations rather than averaging them out, demonstrating robustness in detecting population heterogeneity.

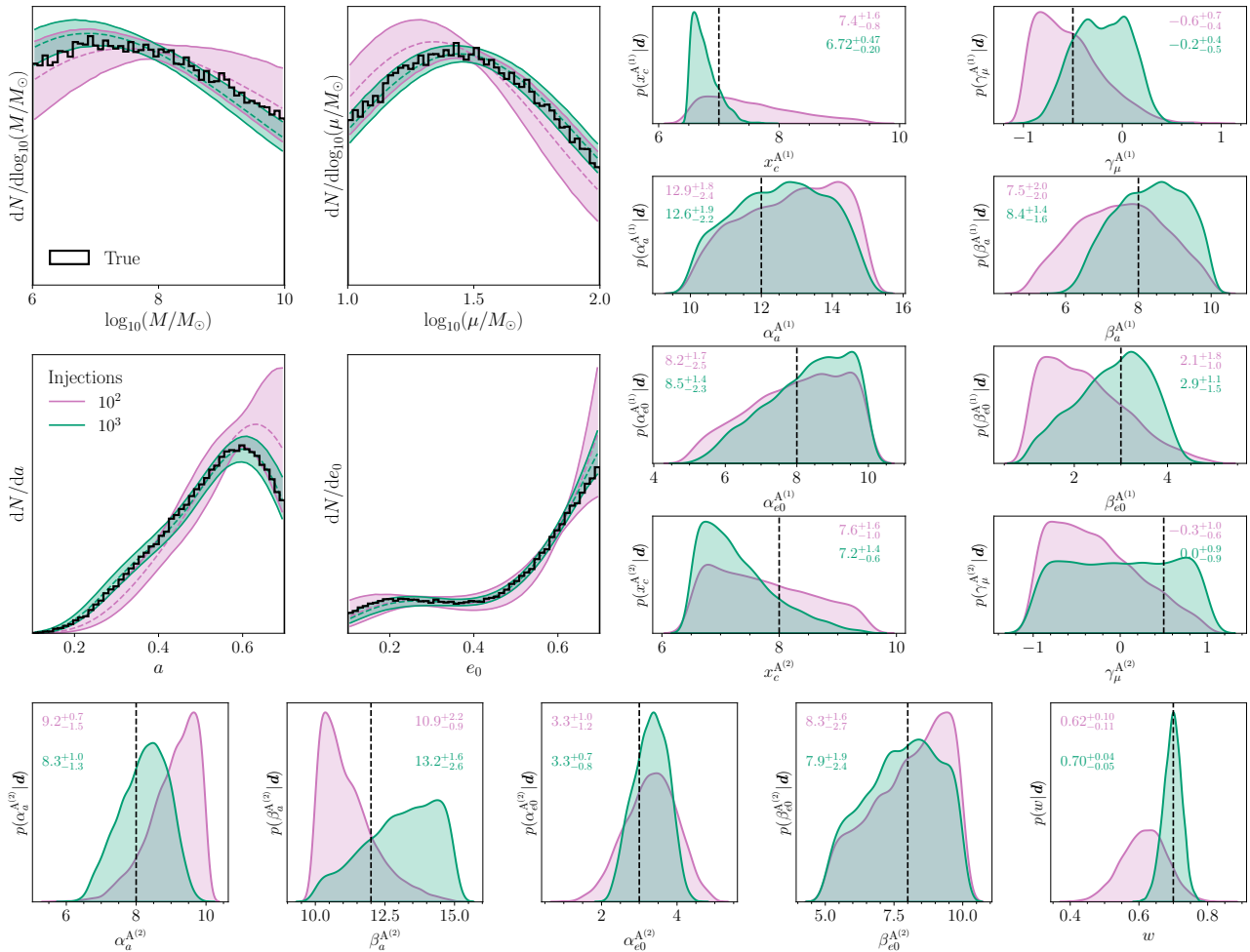


Figure 5. Posterior predictive distributions (*upper left*) and one-dimensional hyperparameter posteriors (*right* and *bottom*) for Model $A^{(1)} + A^{(2)}$. The plotting follows the same structure as Figure 1, where the only difference is the number of hyperparameters used to model the mixed population, where the number of detections is 19, 196 and 1988, for 10^2 , 10^3 , and 10^4 injections, respectively.

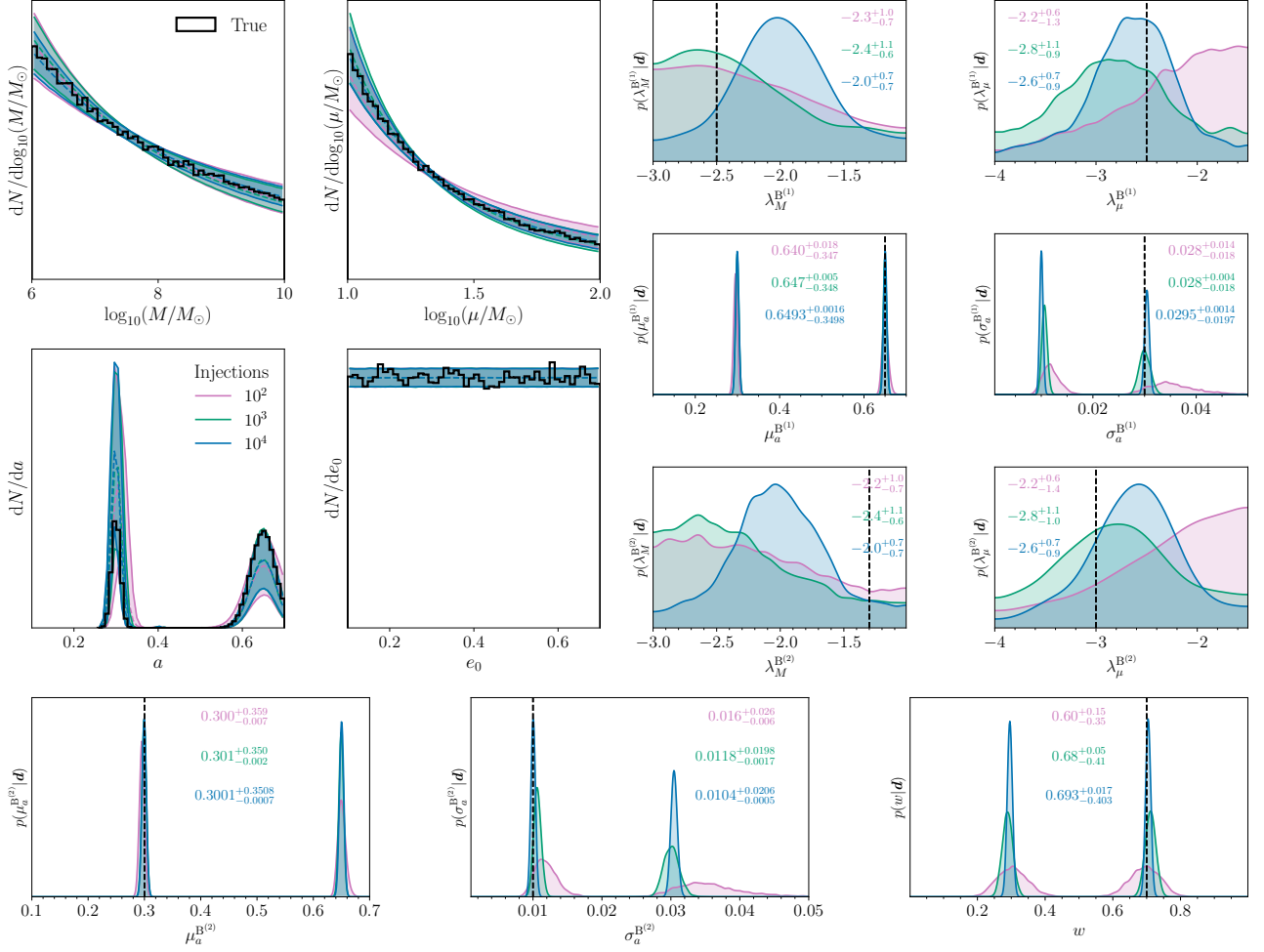


Figure 6. Posterior predictive distributions (*upper left*) and one-dimensional hyperparameter posteriors (*right* and *bottom*) for Model $B^{(1)}+B^{(2)}$. The plotting follows the same structure as Figure 1, where the only difference is the number of hyperparameters used to model the mixed population, where the number of detections is 21, 212 and 2134 for 10^2 , 10^3 , and 10^4 injections, respectively. For bimodal distributions, the median lies in one of the modes, so the uncertainties are asymmetric, with the larger uncertainty reflecting the offset between the modes and the smaller reflecting the width of a single mode.